communications earth & environment

Article

A Nature Portfolio journal

https://doi.org/10.1038/s43247-025-02953-3

Efficient ice multiplication from freezing raindrop fragmentation

Nils Pfeifer[1] ✉, Bernd Mom[2], Dmitri Moisseev[2,3], Susan Hartmann[4], Julian Meusel[5], Corinna Hoose[5] & Maximilian Maahn[1]

Clouds are an important component of our climate system with their life cycle significantly influenced by ice formation. Measured ice concentrations in clouds often exceed the number of ice nucleating particles, a discrepancy attributed to secondary ice processes. However, these processes are not well understood or quantified. One such process, drop fragmentation upon freezing, involves significant uncertainty regarding the number of produced ice particles. Here we identify the occurrence of this process by combining in situ and remote sensing observations during a case of refreezing rain. By categorizing the in situ imagery, we estimate that between 1.2 and 6.1 secondary ice crystals are produced per drop. Drops between 0.5 and 1 mm in diameter were found to be particularly prone to breakup. These results highlight the effectiveness of droplet fragmentation and provide valuable insights for improving the representation of this process in atmospheric models.

Mixed-phase clouds are a widespread and critical component of our climate system[1]. Accurate representation of these clouds in weather and climate models is therefore essential for reliable prediction of Earth's radiation budget, local and global precipitation distribution and the degree of future global warming[2,3]. The life cycle and the optical characteristics of mixed-phase clouds are significantly influenced by ice formation processes. The observed discrepancy between ice nucleating particle (INP) and ice particle number concentrations [e.g., refs. 4–6] in mixed-phase clouds has led to the concept of secondary ice production (SIP). This refers to a collection of processes that enhance the number of ice crystals without the need for INPs[7,8]. Despite their importance, the mechanistic understanding of these processes is limited, and the quantification of all SIP processes is inconsistent and represents a major challenge within cloud microphysics. Current parameterizations of SIP are based on sparse experimental studies, which partly contradict each other[8,9]. The significance of each process in relation to the others has also not been established yet[7]. This makes the unambiguous identification of active SIP processes in real clouds a priority of current research. One of the earliest proposed SIP processes is drop fragmentation upon freezing (DFF)[10]. During this process, a drop will form an ice shell on the surface, encapsulating liquid. As the freezing progresses, ice expanding inwards increases the internal pressure, which can eventually cause the shell to crack or bulge and release ice fragments that form secondary ice[11]. Recent laboratory studies[12,13] have identified four distinct mechanisms during drop freezing (bubble burst, jetting, breakup, and cracking), that can lead to the production of ice splinters in typical atmospheric conditions. The frequency of occurrence of these mechanisms is dependent on drop size and environmental conditions such as air temperature, solute content, sedimentation velocity, and humidity, but, like for other proposed SIP mechanisms, it is unclear how many ice particles are created per freezing drop[8,12,13]. SIP during DFF can occur during the refreezing of rain, where liquid precipitation, falling through a layer with temperatures below 0 °C, freezes into ice pellets[14]. Ice pellets have been regularly observed alongside pristine ice crystals[14–18], suggesting the production of ice splinters in the process, which then can grow to additional ice crystals. In vertical cloud radar observations, refreezing layers can be identified by a distinct signature[19] in the linear depolarization ratio (LDR)[16], a radar variable sensitive to nonsphericity and melting of hydrometeors. Signatures like this were further investigated using radar spectra of LDR, which revealed coexisting populations of hydrometeors with different sedimentation velocities[20,21]. Because cloud radars are able to perform continuous measurements, they can be used to obtain statistically relevant datasets[22]. However, the identification and quantification of the underlying processes remains a challenging issue, because of the indirect nature of radar measurements. This disadvantage can be partly compensated by combination with ground-based in situ observations[23,24], which enable continuous quantification and reveal fingerprints of ice formation processes[25–27].

In this study, we examine a refreezing rain event with strong indications of occurring DFF in Hyytiälä, Finland, on 16 February 2024, using

[1]Leipzig Institute for Meterology (LIM), Leipzig University, Leipzig, Germany. [2]Institute for Atmospheric and Earth System Research/Physics, University of Helsinki, Helsinki, Finland. [3]Finnish Meteorological Institute, Helsinki, Finland. [4]Department of Atmospheric Microphysics, Leibniz Institute for Tropospheric Research, Leipzig, Germany. [5]Institute of Meteorology and Climate Research Troposphere Research, Karlsruhe Institute of Technology, Karlsruhe, Germany.
✉e-mail: nils.pfeifer@uni-leipzig.de

such a combination of measurements. Our aim is to quantify the effectiveness of SIP. Main focus will be on ground-based in situ measurements conducted by the Video In Situ Snowfall Sensor (VISSS)[28] and radar measurements by a 94 GHz cloud radar[29], which are used to develop a timeline of the event. Based on a simple classification, the occurring hydrometeors are divided into subpopulations, allowing us to perform a quantification and a geometrical analysis of the fragmenting drops.

Results

Refreezing rain case

A timeline of the secondary ice formation event on February 16, 2024 (all times given in UTC) reveals four phases of precipitation shown in Fig. 1. Phase I begins at 14:00 with standard snowfall conditions and the formation of a melting layer at ~700 m[30]. In situ images captured by the VISSS (Fig. 1c) depict predominantly small, irregular, or elongated shapes. Phase II starts at 14:30, marked by the onset of refreezing, visible in LDR values at altitudes below 500 m[16]. During this phase, number concentration and particle size distribution (PSD) at the ground remain relatively constant, except for the emergence of rain-sized hydrometeors (~1 mm) in the PSD at 15:15, reaching values of $\sim 10^7$ m^{-4}. In situ images show (completely or partially) melted snow that has collapsed into a spherical shape, or ice pellets resulting from refreezing. A considerable proportion of the shapes are of hemispherical character, which can also be assumed to be frozen. Columns are also observed. The height of the refreezing layer descends around 15:00 but rises again and stabilizes above 500 m for phase III at 15:30. It is characterized by a significant peak in number concentration reaching over 40.000 hydrometeors per cubic meter between 15:50 and 16:40. In addition, PSD values exceed 10^8 m^{-4} for small hydrometeors (<0.5 mm) during that phase. In situ images show that columns, aggregates of columns, as well as ice lollies, defined as ice columns with a droplet attached to one end[31], become the dominant particle shapes during this phase. Finally, phase IV begins around 17:00, marked by the dissipation of the refreezing signature, a stabilization of number concentration compared to phase III, and a transition to rain.

Occurrence of raindrop fragmentation

Here, we show how the columnar ice mainly observed during Phase III grew from ice splinters formed by DFF (Fig. 2). Due to the melting at 1500 m, the observed columnar ice must originate from the refreezing layer (Fig. 2). It cannot be caused by primary ice production by active INP because the concentration of INP in February at the site is typically below 10^{-2} INP per standard liter at −6 °C[32]. This is several orders of magnitude lower than the concentrations measured by the VISSS (temporarily >40/l), indicating that the observed ice splinters are related to SIP. The extent of the snowflakes' melting is discussed in section 1.2 of the supplementary information, with the main result that all snowflakes collapse into drop shape (as evident from radar observations), but at least some of the larger drops still contain ice. After leaving the melting layer, these drops immediately start to refreeze, resulting in DFF with different deformation types [see ref. 12]. Three of the described deformations could also be observed in the VISSS images. The samples in Fig. 2c show spicules and bulges with a wide range of sizes, thicknesses and orientations, which are characteristic of the bubble bursting process. Hemispheres, typically resulting from complete breakup (illustrated in Fig. 2d) were the most prevalent deformation, and are present in all visually verifiable size bins. The rare particles that were identified as resulting from incomplete breakup are depicted in Fig. 2e. At present, the processes of jetting, cracking and bubble burst without bulging cannot be identified because they leave no visible fingerprint that can be detected by the VISSS.

This fragmentation produces ice splinters, which can collide with other supercooled drops and cause them to freeze and fragment, initiating a cascade as shown in refs. 17,33, or grow to columns by vapor deposition, leading to the observed high number concentration at the ground. This process is also supported by the analysis of the Doppler spectra (Supplementary Fig. 1 and Section 1.2 in the supplementary information). The temperatures recorded by the radiosonde launched at 16:18 (Fig. 2) lie only marginally in the temperature range assumed for rime splintering (−8 to −3 °C,[34]). Furthermore, the absence of rime on the surface of the observed particles (Fig. 1c) indicates that rime splintering cannot be a major contributing factor. Also, we are outside of the temperature range of the

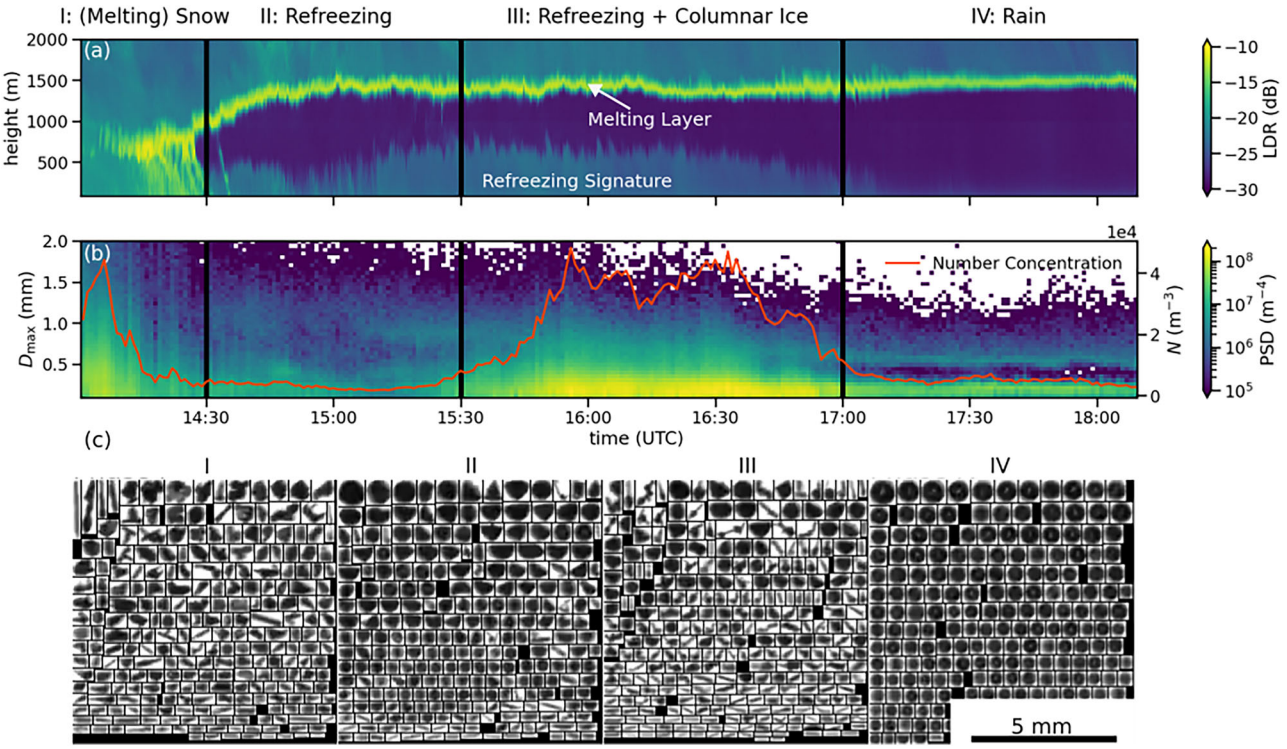

Fig. 1 | Observations of the refreezing event from radar and in situ perspective. a LDR measurement. **b** PSD and total number concentration as measured by the VISSS. **c** Random sample of the particles observed by VISSS during the individual phases.

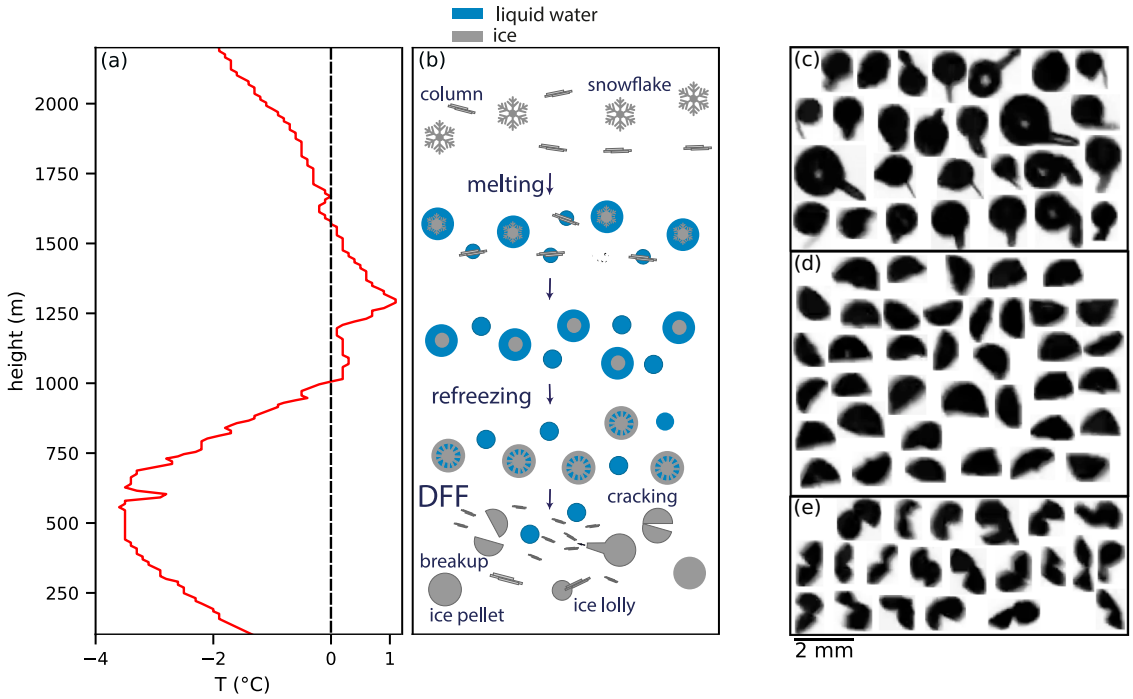

Fig. 2 | Temperature profile, conceptual sketch of the occurring microphysical processes, and example images of the three modes of deformation captured during the refreezing event. a The temperature (red) was measured by a radiosonde launched at 16:18 UTC and is compared to 0 °C (black, dashed). The humidity measurement showed an unrealistic, static value during the ascent through the refreezing layer and is therefore not shown. **b** The conceptual sketch shows the stages of precipitation at different heights during phase III, including the (partial) melting of snowflakes, refreezing into ice pellets and the resulting fragmentation by DFF via breakup, cracking or spicular growth, creating ice splinters. The ice splinters grow into columnar ice, which can collide with droplets to create ice lollies. **c** Hydrometeors that are bulged or show a spicular. **d** Hemispherical particles resulting from complete drop breakup. **e** Incompletely broken drops consisting of two semi-spherical fragments attached together.

dendritic growth range, where collisional breakup is suspected to be most efficient[35]. Sublimation breakup can be excluded because it would result in a decrease in radar reflectivity with decreasing altitude, which is not observed within the refreezing layer. Given all of these considerations, the impact of other SIP processes is likely negligible.

Quantification of ice multiplication

We quantified the SIP by DFF by separating the observed drops/pellets from the columns/aggregates based on their shape (see section "Methods") for sizes larger than 0.41 mm. Here, we use the observed particle concentrations and particle fluxes. The concentration of drops/pellets remains low throughout the three phases (Fig. 3a). In contrast, the concentration of columns/aggregates, which is close to 0 for phases II and IV, demonstrates a prominent increase during Phase III with a distinct maximum (~10^4 particles per m^3) occurring shortly before 16:00, implying a high activity of SIP in this period. The number concentration of the hydrometeors that are too small for the developed classification is displayed in Fig. 3b and shows a clear correlation to that of columns/aggregates, but is higher by a factor of ~4. The fluxes of the individual populations (Fig. 3c, d) show a similar pattern. As the sedimentation velocities of the columns/aggregates and small particles are lower than that of drops/pellets the substantial differences in concentration are to an extent counterbalanced, but Phase III remains predominantly characterized by columnar and small ice. Based on the relatively constant number of drops/pellets at the ground, ratios of the particle fluxes can be used to define an upper and lower limit of how many ice splinters a freezing drop produces on average during the course of the event (Fig. 3c) as outlined in section "Quantifying secondary ice production". The lower limit is based only on particles larger than 0.41 mm and approaches a value of 2.81 at the maximum, while the upper limit reaches a maximum of 13.12, assuming that the small particle concentration is dominated by secondary ice. Both time series show the most activity during Phase III. These time-resolved ratios might be influenced by the size-dependent fall times of the particles, although the concentration of drops/pellets remains relatively constant. Therefore, we also obtain the ratios of the time-integrated fluxes, yielding 1.2 for the lower and 6.1 for the upper limit, as a constraint on the number of ice splinters produced per freezing drop during Phase III as a whole.

Breakup process

The columns/aggregates and drops/pellets classes, along with the *hemispheres* resulting from breakup as a subclass (section "Quantifying broken ice pellets"), were used to calculate individual, time-resolved PSDs (Fig. 4). In Fig. 4a, the population of rain-sized drops (onset 15:10, ~1 mm) that has previously been identified in the total PSD (see Fig. 1b) can also be observed during Phase III. In addition, clusters of smaller drizzle drops (<0.5 mm) are present at the lower end of the depicted size range at 14:50, at 15:40, and between 16:00 and ~16:40. The hemisphere PSD depicted in Fig. 4b overlaps mainly with the observed rain drops from the drop/pellet class. Hemispheres are not observed anymore after the transition to rain. The columns/aggregates class is mainly observed in small-size bins during Phase III, where values of 10^7 m^{-4} are exceeded. Relevant concentrations for larger size bins (>1 mm) are also only observed between 15:30 and 17:00, correlating with the occurrence of hemispheres and the highest breakup fraction. Another cluster of columns/aggregates is visible during the beginning of Phase II, but it does not reach the magnitude of the Phase **III** maximum.

The correlation of a high breakup fraction with the peak in ice multiplication suggests that complete breakup could be a potentially important drop fragmentation mechanism for the case. Therefore, we investigated the *hemispheres* subclass further by calculating a size-dependent breakup fraction as described in "Quantifying secondary ice production". The time frame between 15:30 and 16:30, where this breakup fraction is most stable (between 10 and 15 %, Fig. 4b), is used to generate Fig. 5, which shows a size histogram of the drop/pellet class and the complete breakup fraction for the individual size bins. A bimodal size distribution corresponding to rain and drizzle populations, as well as a distinct maximum in breakup fraction of

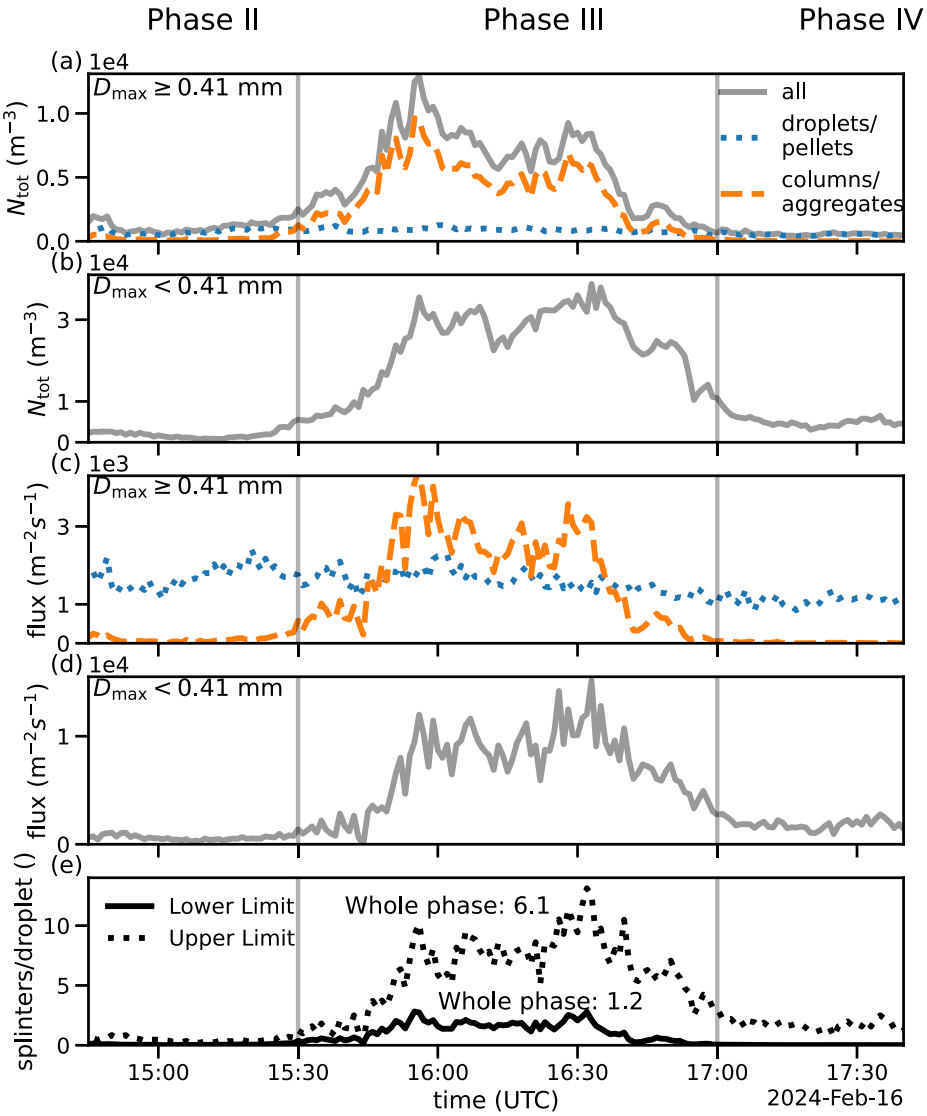

Fig. 3 | Number concentrations and particle fluxes of the defined hydrometeor classes, along with the upper and lower limits of the number of splinters generated per drop. a Concentrations of all (gray), drops (blue, dotted) and columnar ice (orange, dashed) for sizes larger or equal 0.41 mm. **b** Concentration of all hydrometeors observed in size bins <0.41 mm. **c** Particle fluxes of all (gray), drops (blue, dotted) and columnar ice (orange, dashed) for sizes larger or equal 0.41 mm. **d** Particle flux of all hydrometeors observed in size bins <0.41 mm. **e** Upper and lower limits of splinters per drop obtained using the particle fluxes as described in section "Quantifying secondary ice production".

30% around 0.5 mm are observed. For smaller-size bins, the values drop quickly to 12% at 0.46 mm, while for larger drops, the breakup fraction gradually declines, with 1.2 mm drops still breaking with a probability of 15%. It is noticeable that especially rain drops in the range of 0.5 to 1 mm have a high breakup fraction (above or close to 20%).

Discussion

The main goal of this study is to quantify SIP through DFF during the occurrence of refreezing rain based on observations. The number of columns/aggregates that reach the ground during Phase III is in total 1.2 times the number of drops when using only classified particles, when time-integrating the fluxes. This number increases to 6.1 when assuming small particles are dominantly created by SIP (cf. Fig. 3c), which is motivated by the correlation of the concentration of small drops with the concentration of columnar ice (Fig. 4). In comparison[13], observed an average of 2.4 ice splinters produced by 300 µm freely falling drops during breakup for mostly much colder temperatures in a moist environment. This value has to be considered as a lower limit as well, given the technical limitations of the detection of small ice splinters. Despite the fact that the drop size and temperature do not match our observations, there is nevertheless an agreement in the estimated number of ice splinters produced. Older lab studies that have been aggregated in ref. 9 report far lower numbers (e.g., 0.14 and 0.009 fragments per frozen drop for −5 °C), values again at least in part attributable to the difficulties of splinter detection. In contrast, in a field study with similar temperature conditions (>−3 °C), concludes that a 200 µm droplet produces 18 secondary ice particles during DFF, which still has to be regarded as an lower limit[27]. Despite the disagreement in effectivity, the activity of the process observed at relatively high temperatures could be confirmed, which is significantly warmer than in other studies (e.g., −6.7 °C, respectively −8.9 °C for ref. 14). This is a key finding of this study, potentially relevant for explaining why SIP is regularly observed close to the melting layer[36]. For a case of refreezing rain close to Montreal, Canada, similar to the presented case, ref. 14 found that five to eight fragments of ice are produced per drop during DFF, determined through analysis of airborne data. This consistency in estimated efficiency using a different set of instruments at another geographical location indicates that the assumptions of this study are valid and the results are not specific to this case study. Additionally, in ref. 14, two available parametrizations of DFF were found unable to reproduce the observed numbers, which demonstrates the need for adjusted representations of DFF in models. The effect of aggregation on the results is difficult to quantify. Since the columns/aggregates class includes aggregates of columns that are counted only once, the actual number of columns will be higher than estimated in all cases. The observed ice lollies can be regarded as evidence for collisions between supercooled drops and growing ice splinters. The freezing of drops initiated by these collisions could potentially result in further DFF, thereby initiating a cascading process as described in ref. 17. These collisions would result in the loss of columns, which would contribute further to an underestimation of

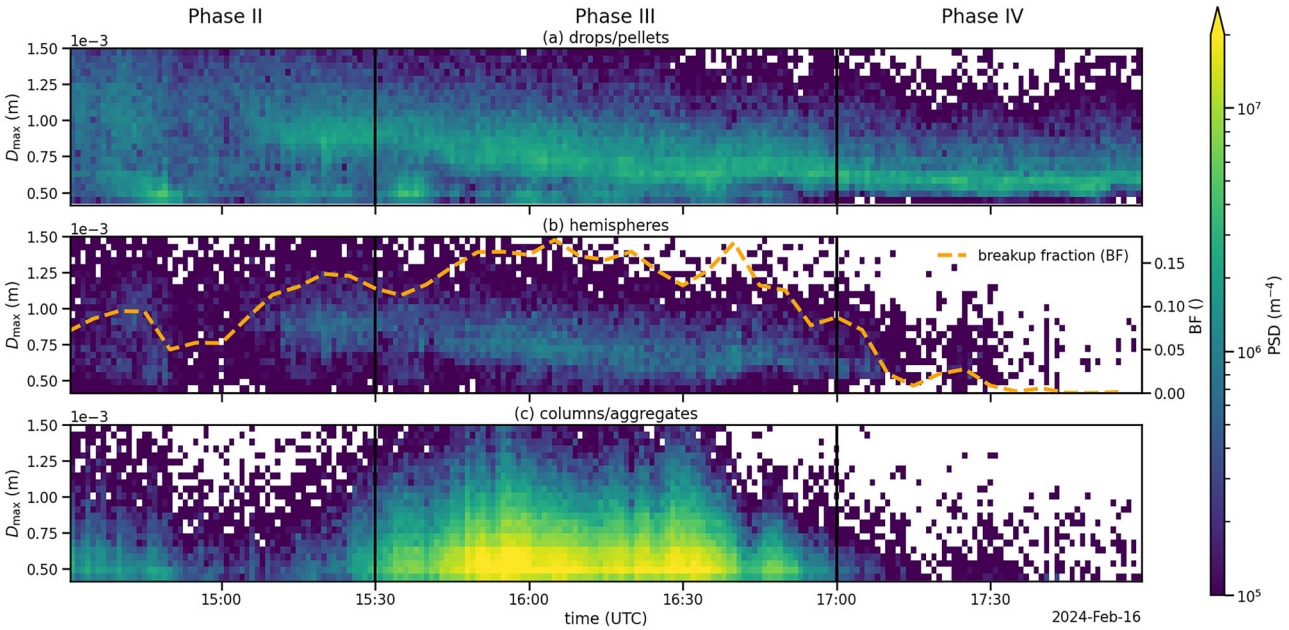

Fig. 4 | PSDs of the hydrometeor classes during the event. a PSD of drops/pellets. **b** PSD of hemispheres. **c** PSD if columns/aggregates. PSDs are calculated using the classifications introduced in the methodology section "Methods". **b** also shows the breakup fraction (5-min running average for smoothing) defined in section "Method" for the event.

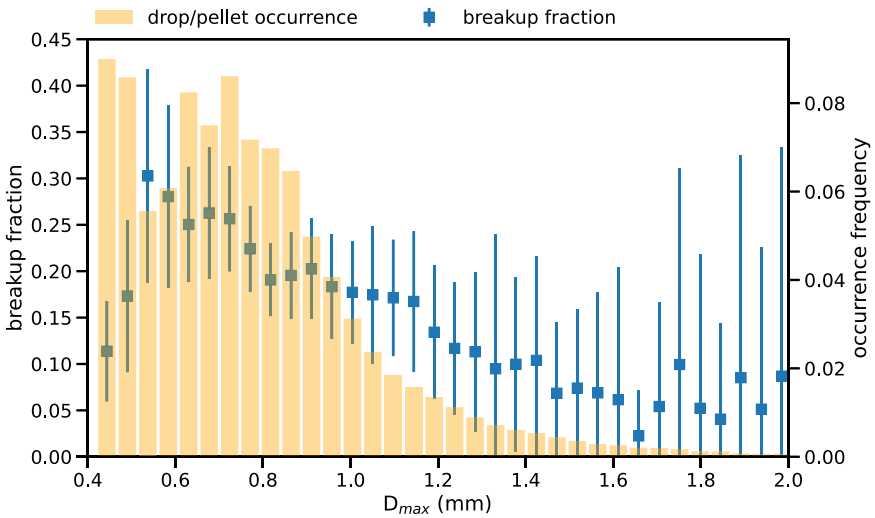

Fig. 5 | Normalized size histogram of the drops/pellets class (yellow) and the complete breakup fraction in the same size bins. Size bins are based on the resolution of the VISSS (46.7 µm). The breakup fraction was obtained using the concentration of the hemisphere and the drop/pellet classes between 15:30 and 16:30. The error was calculated from the standard deviation of the hemisphere concentration for the individual size bins within this time frame.

the secondary ice production. However, the frequency of such collisions remains uncertain and via testing (assuming that each ice pellet has collided with an ice splinter) this effect was found to be to be minor. The absence of a measured humidity profile for the subfreezing layer leads to further ambiguities, e.g., regarding the effect of a potential evaporative cooling on the droplets. In summary, it must be recognized that the estimation of secondary ice production is subject to some uncertainty. In order to accurately measure the number of secondary ice particles produced by DFF, well-controlled laboratory experiments are required. Further, to account for interaction of different hydrometeors (for example, collisions between ice splinters and unfrozen supercooled droplets) leading to glaciation in a turbulent flow field, detailed turbulence resolving-models are the method of choice, especially to model the cascade effect of ice multiplication. Regarding the affinity to breakup, the general trend observed in lab studies is that larger droplets are more prone to shatter[8,12]. In contrast to these findings, we have seen a maximum probability of breakup between 0.5 and 1 mm. For larger diameters, the fraction of broken drops decreases again. A key factor might be the possibly incomplete melting of the largest drops. In ref. 37, a breakup fraction of ~20% is reported for a similar case of refreezing, as observed through macrophotography of ice pellets on the ground, within the size range of 0.5 to 1 mm. Consistent with the study at hand, a decrease in the breakup fraction is observed for larger sizes. For other events, that are completely dominated by partial melting[37] find almost no fracturing for all sizes. This evidence suggests that the degree of melting is crucial for the activity of the DFF. Conversely, for smaller drops that do not contain ice, it is possible that no freezing process is initiated, which could explain the observed decrease in breakup fraction for smaller sizes. Other relevant factors could be humidity and ventilation. Keinert et al. (2020)[13] report a breakup frequency of ~15% during lab experiments with 300-µm droplets of pure water at −5 °C in a moist airflow. For the smallest size bin (~0.41 mm), we observe about 12% of breakup. Again, a qualitative agreement is found here, even though the parameters of the setup differ. The SIP is only highly

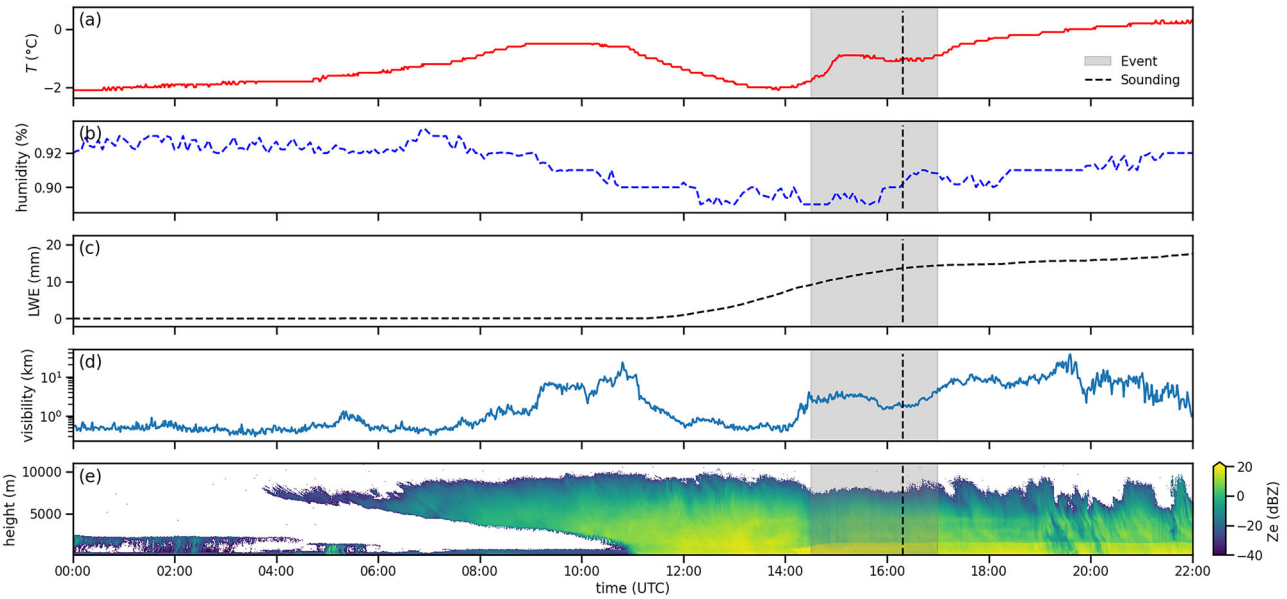

Fig. 6 | Meteorological conditions on the 16th of February 2024. a Time series of 2 m temperature at the measurement site. **b** Time series of 2 m relative humidity at the measurement site. **c** Time series of the measured cumulative liquid water equivalent (LWE) precipitation at the measurement site. **d** Time series of the visibility at the measurement site. **e** Time-height plot of the reflectivity *Ze* showing the passage of the cloud system responsible for the precipitation during the day of the event. The time frame of the event is indicated with a gray box and time of the radiosounding is marked with a dashed black line.

active for a limited time frame of ~1.5 h, which supports the general finding from ref. 22 that secondary ice events are transient. One of the key questions regarding the timeline of the event is why the efficiency of the process during Phase II is comparatively low, despite the conditions not being significantly different from those of Phase III, where a high efficiency is observed. One potentially major influence identified through the analysis of the PSDs is that drops, which are prone to breakup (0.5–1 mm), are more numerous during Phase III (Fig. 4). This suggests that larger rain drops could play a more significant role in the process of DFF than smaller drizzle drops, aligning with the general observation that bigger droplets produce more splinters when fragmenting. Another possible influence is the potentially different degree of partial melting that occurs during Phase II. As discussed previously[37], we found almost no fracturing and bulging in cases involving partial melting, which can be assumed to be connected to the lower efficiency of SIP. Moreover, it is possible that columnar ice may be present prior to the increase of the total number concentration observed by the VISSS„ which has not grown to a size sufficiently large for detection. The resolution of the VISSS (46.7 µm), which prevents the reliable detection of hydrometeors smaller than 93.4 µm, is the main limitation for the analysis. Additionally, splinters produced aloft that are initially suspended or fall at a very low velocity will be detected on the ground with a delay. The presented methodology for quantifying SIP from a ground-based perspective can aid in evaluating parameterizations for DFF from a unique event-based view. Additionally, the method has the potential to be extended to the process of rime-splintering, by distinguishing between graupel and small ice particles with the same approach. Future studies should apply this method to other cases to obtain additional data points in the vast parameter space.

Methods

Location and instrumentation

We used data from Hyytiälä, Finland (147 m above mean sea level, 61.8°N, 24.29°E) during January and February 2024. In the following, all altitudes are expressed in relation to the ground level of the site and all times are given in coordinated universal time (UTC).

Ground-based in situ measurements were performed with the third generation of the VISSS. For a detailed description of the technical details of the device and its data processing, refer to ref. 28. This device is a system composed of two cameras arranged at a 90° angle to each other, so that they constrain an observation volume (47.1 × 47.1 × 58.9 mm), which enables the accurate calculation of ice crystal number concentrations. The utilization of telecentric lenses ensures the elimination of sizing errors due to different object distances. Videos are captured at a frame rate of 220 Hz and a resolution of 46 µm, and consecutive frames that exhibit movement are saved as raw data. In the data processing chain, individual hydrometeors are reliably identified in the videos, if they are equal to or larger than two pixels in size, i.e., 93.4 µm. These are geometrically analysed and the resulting properties are saved, along with the position and the time of recording. The perspectives of both cameras are then combined using a probabilistic comparison of selected attributes, enabling the identification of hydrometeors observed from two sides within the observational volume. In order to calculate sedimentation velocities, particles are tracked through multiple frames based on the prediction of future positions. The final processing step is to switch from particle properties to time-resolved statistics. The resulting datasets contain the calibrated concentration, particle size distributions and the statistics of the hydrometeor properties.

A 94 GHz dual-polarization frequency-modulated continuous-wave Doppler cloud radar[38] is installed at the site. It is oriented vertically and is capable of measuring spectral moments, LDR (minimum observable LDR around −30 dB), and dual-polarization Doppler spectra. In this study, we analyze reflectivity and spectral observations recorded on the 16th of February 2024[29]. For the range of 102 to 996 m, which is most relevant for the analysis in this study, a range resolution of 25.5 m, a Doppler unambiguous velocity of 10.24 m/s and a Doppler spectral resolution of 0.02 m/s apply. For an in-depth description of the cloud radar, consider, for example, ref. 20.

Radio soundings were conducted utilizing *GRAW DFM-17* sondes, which measured profiles of temperature and humidity. At the ground, measurements of temperature, humidity, wind and pressure are observed by a weather station[39].

Case

On February 16, 2024, a warm front linked to a Scandinavian low-pressure system brought stratiform precipitation to the measurement site. Surface temperatures rose from −2 °C at 14:00 UTC to 0.5 °C by midnight, accompanied by 20 mm of liquid water equivalent precipitation, transitioning from snow to rain (Fig. 6a). Radar reflectivity data showed cloud development starting around 6:00 UTC at 7500 m with precipitation beginning at ~11:00

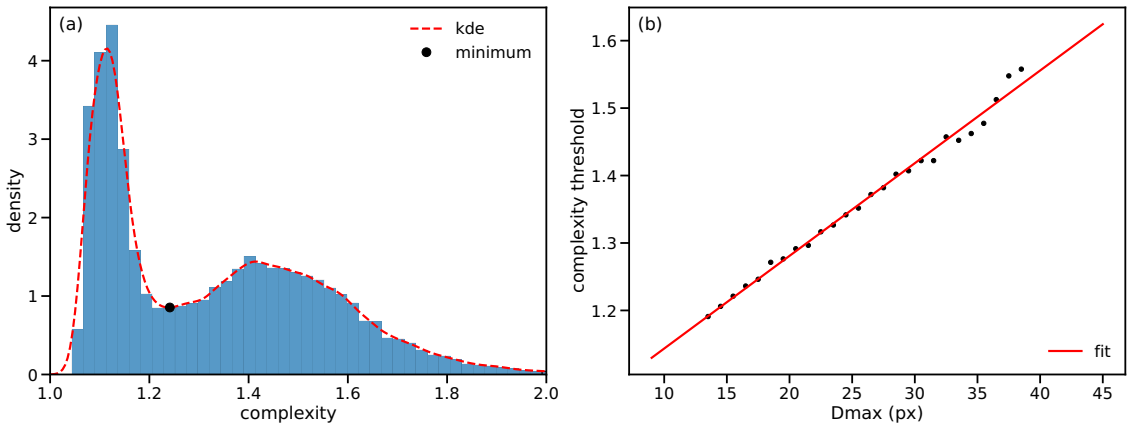

Fig. 7 | Visualization of the method applied to separate between drops/pellets and columns/aggregates. a Density histogram of particle complexity χ for the [13, 14] px size bin, including kernel density estimation (kde) and the detected local minimum. **b** Values of the local minimum plotted against the size of the particles and the performed linear fit (intercept: 0.9877, slope: 0.0146, R^2: 0.9954).

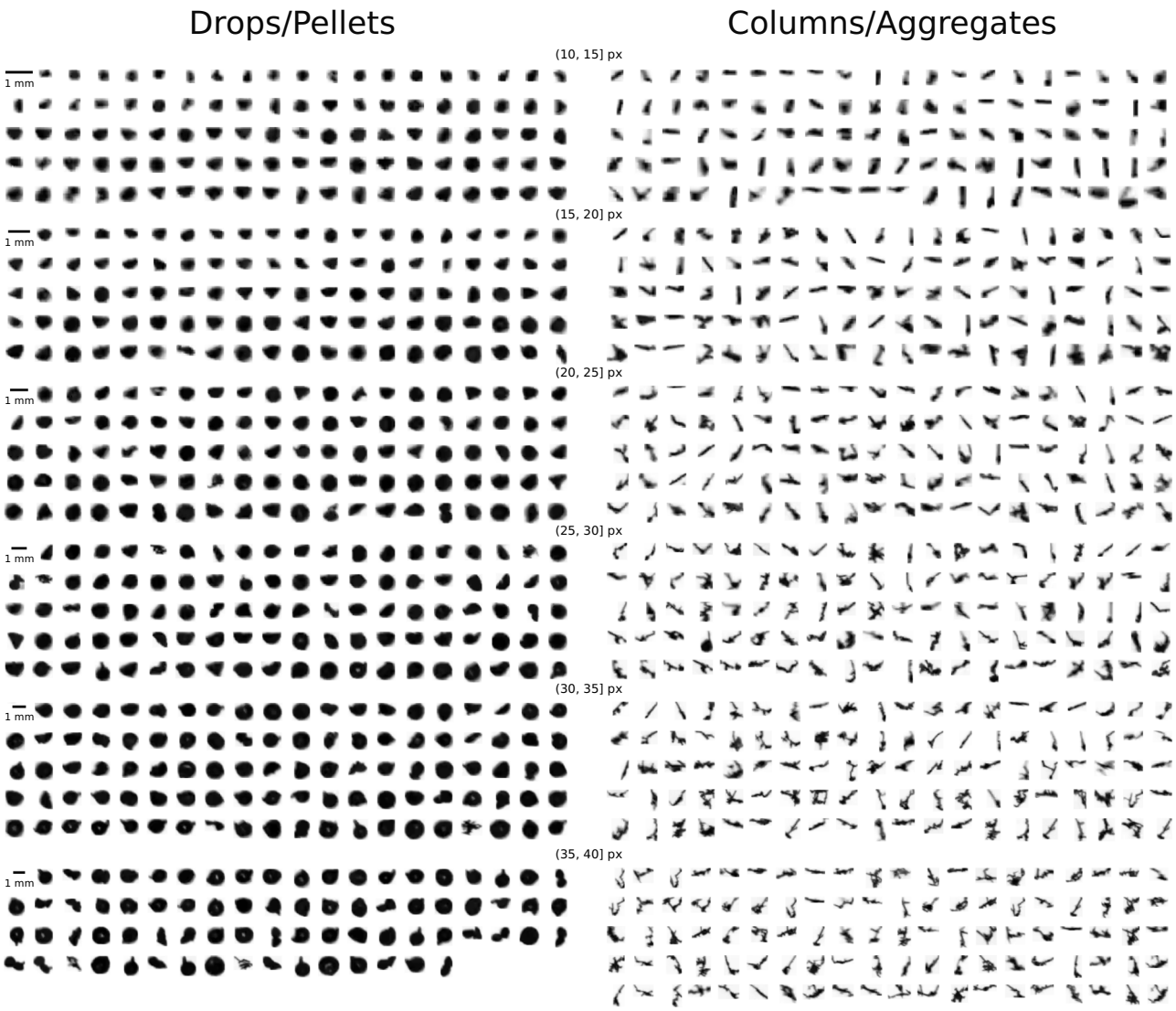

Fig. 8 | Example for the classification of drops/pellets (left) and columns/aggregates (right). The pictures shown here were recorded between 16:20–16:30 UTC. They are shown in 5 px size bins, were each pixel corresponds to 46 µm (VISSS resolution). Each grid cell shows 100 particles of that size bin and class. If the class for a respective bin contains more than 100 particles, random sampling is used. The apparent repetition of identical particles is the result of them being captured multiple times in consecutive frames.

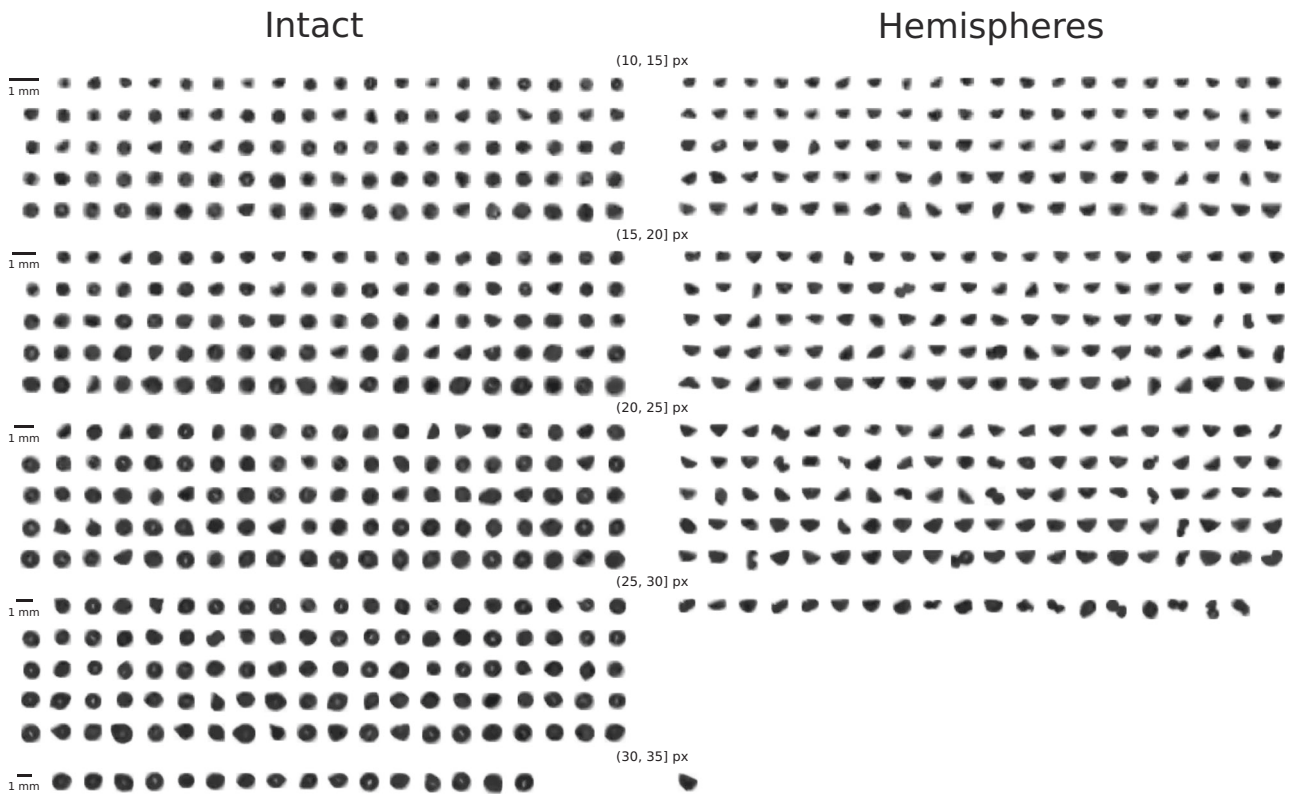

Fig. 9 | Example for the classification of hemispheres (right) and intact ice pellets (left). The pictures shown here were recorded between 17:00 and 17:10 with a threshold of 0.75 in aspect ratio used to distinguish between the classes. Each grid cell shows 100 particles of a 5 px size bin and class.

UTC (Fig. 6b). The humidity and visibility observations indicate no fog during the event, as their values remain below 95% and above 1 km, respectively.

Separating ice pellets and columnar ice

The initial precipitation during the presence of refreezing signature (Phase II), comprises liquid drops and ice pellets, which can be spherical, deformed, broken, or bulged. This class will be called drops/pellets in the following. Starting from 15:30 UTC until 17:00 UTC, single columns (or needles), ice lollies and aggregates are reaching the ground (Fig. 1c). Subsequently, these three particle types will be collected under the label columns/aggregates. To distinguish between drops/pellets and columns/aggregates, a classification based on the hydrometeor geometry was developed. For this purpose, the complexity of a particle, defined in ref. 40 as

$$\chi = \frac{P}{2\pi r_{\mathrm{eq}}}, \tag{1}$$

with the perimeter P and the area equivalent radius r_{eq}, was calculated for all hydrometeors observed during the event. For a completely round particle χ equals 1 and this value increases with deviation from a spherical shape. The resulting dataset was then aggregated into bins based on the maximum diameter of the particle in pixels (~46 µm per pixel). For each of these bins, a density histogram of χ was plotted. Starting from a size of 13 up to 40 pixels, these histograms revealed a bimodal distribution, with each mode corresponding to one of the two classes. Hydrometeors larger than 40 pixels were too sparse to apply this method. Below 13 pixels, the bi-modality disappeared, presumably due to resolution limits. For the size bins between 13 and 40 px, a Gaussian kernel density estimation of the χ-histogram was performed, and its local minimum, as the value that best separates both classes, was detected using the *scipy* library[41]. The values of these minima were plotted against the maximum particle diameter and extrapolated to smaller and larger sizes using a linear fit (Fig. 7).

This fit was performed multiple times on random subsamples of the minima, obtained through bootstrapping, to derive a set of slopes and intercepts. It was found beneficial to use the values at the 5th percentile of this set for better separation of the two classes. This resulted in

$$\begin{aligned} \chi_{\mathrm{thresh}} &= aD_{\mathrm{max}} + b \\ a &= 0.0131/\mathrm{px} \\ b &= 0.9921 \end{aligned} \tag{2}$$

as size-dependent threshold for D_{max} given in pixels, with every hydrometeor with a complexity larger than this threshold being classified as columns/aggregates and those with a lower complexity being regarded as drops/pellets. An example of this classification is shown in Fig. 8. Based on the above calculated linear fit, the error of the classification between 13 and 41 px is estimated to be below 5%. Even for particle sizes between 9 and 13 pixels and larger than 40 pixels the error is estimated to be below 5%, as confirmed by manual inspection. 9 px corresponds to approximately 0.41 mm, as the lower limit of the classification. Using this threshold, time series of individual concentrations, PSDs and velocity distributions of the two classes can be calculated.

Quantifying broken ice pellets

Keinert et al.[13] observed that droplets typically break into two equally large fragments. Thus, the drops/pellets class is filtered for hemispheres as a subclass, i.e., every hemisphere also belongs to the drop/pellet class. Hemispheres are characterized by an aspect ratio (the ratio of width and length) of ~0.5, whereas intact drops have an aspect ratio close to 1. In the VISSS data processing, the aspect ratio is calculated by fitting a rectangle to the shape of the observed hydrometeor and dividing the width and length of this rectangle. Through the application of a threshold that is based on the minimum value of the two camera perspectives of this aspect ratio, the drop category can be effectively filtered to isolate those exhibiting hemispherical shapes by setting a threshold value of 0.75. It is important to note

that not all breakup events yield perfectly hemispherical shapes. Some broken ice pellets will remain classified within the broader drops/pellets category. For larger size bins, low aspect ratios are also achieved by ice pellets with long spicules, which are therefore miscategorised. The same applies to incompletely broken ice pellets. On the other hand, hemispheres with spicules can, in turn, cause aspect ratios close to 1 and are therefore wrongly classified. For smaller-size bins, the hemispherical shape is increasingly hard to identify correctly, with no clear bias towards false positives or false negatives. An example of such a categorization is shown in Fig. 9. By visual inspection of plots like Fig. 9, an overall classification accuracy of 20% is assumed here.

Quantifying secondary ice production

For the classes defined in the two preceding sections, individual fluxes can be calculated using the PSDs and velocity distributions observed by the VISSS, i.e.,

$$\phi_i(D) = \mathrm{PSD}_i(D) v_i(D), \tag{3}$$

where i can stand for any defined subpopulation of the observed hydrometeors. SIP by DFF is then quantified by introducing size-independent number fluxes

$$\Phi_i = \int_0^\infty \phi_i(D) dD \tag{4}$$

for the four classes drops/pellets, columns/aggregates, hemispheres and small particles. The following two ratios are regarded as upper and lower limits of the number of ice splinters created per freezing drop:

$$\text{Lower Limit} = \frac{\Phi_{\text{columns/aggregates}}}{\Phi_{\text{drops/pellets}} - \frac{1}{2}\Phi_{\text{hemispheres}}} \tag{5}$$

and

$$\text{UpperLimit} = \frac{\Phi_{\text{columns/aggregates}} + \Phi_{\text{small}}}{\Phi_{\text{drops/pellets}} - \frac{1}{2}\Phi_{\text{hemispheres}}}. \tag{6}$$

The lower limit is obtained as the ratio between columns/aggregates and drops/pellets for particles larger than 0.41 mm, assuming that columnar ice is produced by the freezing of the drops. The flux of drops/pellets is reduced by half of the flux of hemispheres, accounting for the fact that a drop splits into two hemispheres. For the upper limit, it is assumed, that all small particles (<0.41 mm) are also produced by DFF.

The breakup fraction is calculated using the concentrations at the ground N_i, via

$$\mathrm{BF} = \frac{\frac{1}{2}N_{\text{hemispheres}}}{N_{\text{drops/pellets}} - \frac{1}{2}N_{\text{hemispheres}}}, \tag{7}$$

again we take into account that single drops break into two hemispheres. Fluxes are not considered here, since they were not found to alter the results considerably.

Data availability

Cloud radar and weather station data were available in the *Cloudnet* data portal[29,39]. Raw in situ data of the VISSS was published via *Pangea*[42]. The time-resolved in situ datasets used in this study are available at https://doi.org/10.5281/zenodo.17434700.

Code availability

The raw in situ data were processed using the open source *VISSSlib* library[43]. The figures of the main manuscript can be reproduced using the Jupyter Notebook given in https://doi.org/10.5281/zenodo.17434749.

Received: 22 July 2025; Accepted: 28 October 2025;
Published online: 21 November 2025

References

1. Mülmenstädt, J., Sourdeval, O., Delanoë, J. & Quaas, J. Frequency of occurrence of rain from liquid-, mixed-, and ice-phase clouds derived from A-Train satellite retrievals. *Geophys. Res. Lett.* **42**, 6502–6509 (2015).
2. Korolev, A. et al. Mixed-phase clouds: progress and challenges. *Meteorol. Monogr.* **58**, 5.1–5.50 (2017).
3. Hofer, S. et al. Realistic representation of mixed-phase clouds increases projected climate warming. *Commun. Earth Environ.* **5**, 390 (2024).
4. Koenig, L. R. The glaciating behavior of small cumulonimbus clouds. *J. Atmos. Sci.* **20**, 29–47 (1963).
5. Mossop, S. C. concentrations of ice crystals in clouds. *Bull. Am. Meteorol. Soc.* **51**, 474–480 (1970).
6. Hobbs, P. V. & Rangno, A. L. Ice particle concentrations in clouds. *J. Atmos. Sci.* **42**, 2523–2549 (1985).
7. Field, P. R. et al. Chapter 7. Secondary ice production - current state of the science and recommendations for the future. *Meteorol. Monogr.* https://doi.org/10.1175/AMSMONOGRAPHS-D-16-0014.1 (2016).
8. Korolev, A. & Leisner, T. Review of experimental studies of secondary ice production. *Atmos. Chem. Phys.* **20**, 11767–11797 (2020).
9. Phillips, V. T. J., Patade, S., Gutierrez, J. & Bansemer, A. Secondary ice production by fragmentation of freezing drops: formulation and theory. *J. Atmos. Sci.* **75**, 3031–3070 (2018).
10. Takahashi, C. & Yamashita, A. Shattering of frozen water drops in a supercooled cloud. *J. Meteorol. Soc. Jpn. Ser. II* **48**, 373–376 (1970).
11. Kalita, A. et al. Microstructure and crystal order during freezing of supercooled water drops. *Nature* **620**, 557–561 (2023).
12. Lauber, A., Kiselev, A., Pander, T., Handmann, P. & Leisner, T. Secondary ice formation during freezing of levitated droplets. *J. Atmos. Sci.* **75**, 2815–2826 (2018).
13. Keinert, A., Spannagel, D., Leisner, T. & Kiselev, A. Secondary ice production upon freezing of freely falling drizzle droplets. *J. Atmos. Sci.* **77**, 2959–2967 (2020).
14. Lachapelle, M. et al. Airborne and ground measurements for vertical profiling of secondary ice production during ice pellet precipitation. *J. Atmos. Sci.* **82**, 559–583 (2025).
15. Stewart, R. & Crawford, R. Some characteristics of the precipitation formed within winter storms over eastern Newfoundland. *Atmos. Res.* **36**, 17–37 (1995).
16. Kumjian, M. R., Tobin, D. M., Oue, M. & Kollias, P. Microphysical insights into ice pellet formation revealed by fully polarimetric Ka-band Doppler radar. *J. Appl. Meteorol. Climatol.* **59**, 1557–1580 (2020).
17. Lachapelle, M. & Thériault, J. M. Characteristics of precipitation particles and microphysical processes during the 11-12 January 2020 ice pellet storm in the Montréal Area, Québec, Canada. *Monthly Weather Rev.* **150**, 1043–1059 (2022).
18. Minder, J. R. et al. P-type processes and predictability: the winter precipitation type research multiscale experiment (WINTRE-MIX). *Bull. Am. Meteorol. Soc.* **104**, E1469–E1492 (2023).
19. Kumjian, M. R., Ryzhkov, A. V., Reeves, H. D. & Schuur, T. J. A dual-polarization radar signature of hydrometeor refreezing in winter storms. *J. Appl. Meteorol. Climatol.* **52**, 2549–2566 (2013).
20. Li, H., Möhler, O., Petäjä, T. & Moisseev, D. Two-year statistics of columnar-ice production in stratiform clouds over Hyytiälä, Finland: environmental conditions and the relevance to secondary ice production. *Atmos. Chem. Phys.* **21**, 14671–14686 (2021).
21. Billault-Roux, A.-C. et al. Distinct secondary ice production processes observed in radar Doppler spectra: insights from a case study. *Atmos. Chem. Phys.* **23**, 10207–10234 (2023).
22. Luke, E. P., Yang, F., Kollias, P., Vogelmann, A. M. & Maahn, M. New insights into ice multiplication using remote-sensing observations of

slightly supercooled mixed-phase clouds in the Arctic. *Proc. Natl Acad. Sci. USA* **118**, e2021387118 (2021).
23. Mason, S. L., Chiu, C. J., Hogan, R. J., Moisseev, D. & Kneifel, S. Retrievals of riming and snow density from vertically pointing Doppler radars. *J. Geophys. Res. Atmos.* **123**, 13,807–13,834 (2018).
24. Bukovčić, P., Ryzhkov, A., Zrnić, D. & Zhang, G. Polarimetric radar relations for quantification of snow based on disdrometer data. *J. Appl. Meteorol. Climatol.* **57**, 103–120 (2018).
25. Nagumo, N. & Fujiyoshi, Y. Microphysical properties of slow-falling and fast-falling ice pellets formed by freezing associated with evaporative cooling. *Monthly Weather Rev.* **143**, 4376–4392 (2015).
26. Nagumo, N., Adachi, A. & Yamauchi, H. Geometrical properties of hydrometeors during the refreezing process and their effects on dual-polarized radar signals. *Monthly Weather Rev.* **147**, 1753–1768 (2019).
27. Lauber, A. et al. Continuous secondary-ice production initiated by updrafts through the melting layer in mountainous regions. *Atmos. Chem. Phys.* **21**, 3855–3870 (2021).
28. Maahn, M., Moisseev, D., Steinke, I., Maherndl, N. & Shupe, M. D. Introducing the video in situ snowfall sensor (VISSS). *Atmos. Meas. Tech.* **17**, 899–919 (2024).
29. Moisseev, D. & Petäjä, T. Radar data from Hyytiälä on 16 February 2024. https://hdl.handle.net/21.12132/1.d980ed07e8924e86 (2024).
30. Li, H. & Moisseev, D. Two layers of melting ice particles within a single radar bright band: interpretation and implications. *Geophys. Res. Lett.* **47**, e2020GL087499 (2020).
31. Keppas, S. C., Crosier, J., Choularton, T. W. & Bower, K. N. Ice lollies: an ice particle generated in supercooled conveyor belts. *Geophys. Res. Lett.* **44**, 5222–5230 (2017).
32. Schneider, J. et al. The seasonal cycle of ice-nucleating particles linked to the abundance of biogenic aerosol in boreal forests. *Atmos. Chem. Phys.* **21**, 3899–3918 (2021).
33. Lachapelle, M., Cholette, M. & Thériault, J. M. Effect of secondary ice production processes on the simulation of ice pellets using the predicted particle properties microphysics scheme. *Atmos. Chem. Phys.* **24**, 11285–11304 (2024).
34. Hallett, J. & Mossop, S. C. Production of secondary ice particles during the riming process. *Nature* **249**, 26–28 (1974).
35. Grzegorczyk, P. et al. Fragmentation of ice particles: laboratory experiments on graupel-graupel and graupel-snowflake collisions. *Atmos. Chem. Phys.* **23**, 13505–13521 (2023).
36. Korolev, A. et al. A new look at the environmental conditions favorable to secondary ice production. *Atmos. Chem. Phys.* **20**, 1391–1429 (2020).
37. Lachapelle, M., Thompson, H. D., Leroux, N. R. & Thériault, J. M. Measuring ice pellets and refrozen wet snow using a laser-optical disdrometer. *J. Appl. Meteorol. Climatol.* **63**, 65–84 (2024).
38. Küchler, N. et al. A W-band radar-radiometer system for accurate and continuous monitoring of clouds and precipitation. *J. Atmos. Ocean. Technol.* **34**, 2375–2392 (2017).
39. Moisseev, D. & Petäjä, T. Weather station data from Hyytiälä on 16 February 2024 https://hdl.handle.net/21.12132/1.326dd79dc9e44654 (2024).
40. Garrett, T. J., Fallgatter, C., Shkurko, K. & Howlett, D. Fall speed measurement and high-resolution multi-angle photography of hydrometeors in free fall. *Atmos. Meas. Tech.* **5**, 2625–2633 (2012).
41. Virtanen, P. et al. SciPy 1.0: fundamental algorithms for scientific computing in Python. *Nat. Methods* **17**, 261–272 (2020).
42. Maahn, M., Moisseev, D. & Pfeifer, N. Video in situ snowfall sensor (VISSS) data for Hyytiälä (December 2023 - July 2024) https://doi.org/10.1594/PANGAEA.981869 (2025).
43. Maahn, M. maahn/VISSSlib https://github.com/maahn/VISSSlib (2025).

Acknowledgements

N.P., J.M., C.H., and M.M. gratefully acknowledge the funding by the Deutsche Forschungsgemeinschaft (DFG, German Research Foundation) for the "Evaluating Microphysical Pathways Of midlatitude Snow formation", Project 516261703. SH was also supported by DFG (Project 386137169). B.M. and D.M. were supported by funding from the Horizon Europe program under Grant Agreement No. 101137680 via project CERTAINTY (Cloud-aERosol inTeractions & their impActs IN The earth sYstem). Field work in Hyytiälä was supported by ATMO-ACCESS (ATMO-TNA-4–0000000049). C.H. was also supported by CleanCloud (Clouds and climate transitioning to post-fossil aerosol regime), Horizon Europe grant agreement 101137639. The authors would like to thank the staff of the Hytiälä forest field station, and in particular Pauliina Schiestl-Aalto from the University of Helsinki, for the technical support provided at the measurement site. This work was supported by the Open Access Publishing Fund of Leipzig University. Finally, we would also like to thank the three anonymous reviewers for their constructive feedback.

Author contributions

N.P.: concept; data analysis; methodology; visualization; campaign, writing—original draft; writing— review and editing. B.M.: data analysis—radar data; visualization; campaign; writing—review and editing. D.M.: concept; campaign—enabling; writing—review and editing. S.H.: concept; data analysis—melting time estimation; visualization; writing—review and editing. J.M.: campaign; writing—review and editing. C.H.: funding acquisition; concept; writing— review and editing. M.M.: funding acquisition; supervision; concept; writing—review and editing.

Funding

Open Access funding enabled and organized by Projekt DEAL.

Competing interests

The authors declare no competing interests.

Additional information

Supplementary information The online version contains supplementary material available at https://doi.org/10.1038/s43247-025-02953-3.

Correspondence and requests for materials should be addressed to Nils Pfeifer.

Peer review information *Communications Earth and Environment* thanks Matthieu Lachapelle and the other, anonymous, reviewer(s) for their contribution to the peer review of this work. Primary Handling Editors: Nicola Colombo and Aliénor Lavergne. A peer review file is available.